Oil Shale, 2025, Vol. 42, No. 4, pp. 390–413
doi: https://doi.org/10.3176/oil.2025.4.03

ISSN 0208-189X

Organic-rich shale in Lianggaoshan Formation: study on macroscopic and microscopic mechanical properties and mechanism of influencing factors

Yangbing Li[(a,b)]*, Weiqiang Hu[(a,b)], Litao Ma[(a,b)], Jianqi Chen[(a,b)], Zaizhen Liu[(a,b)], Di Cao[(a,b)], Panpan Li[(a,b)], Chenchen Li[(a,b)]

(a) CNOOC EnerTech-Drilling & Production Co., Tianjin 300452, China
(b) CNOOC Energy Technology & Services Limited Key Laboratory for Exploration & Development of Unconventional Resources, Tianjin 300452, China

Received 4 January 2025, accepted 15 October 2025, available online 20 October 2025

Abstract. *This study investigates the mechanical properties of organic-rich shale from the Lianggaoshan Formation using uniaxial and triaxial tests, nanoindentation, and atomic force microscopy. Key parameters such as elastic modulus and hardness are analyzed with NanoScope Analysis software. The results indicate that flat-laminated shale outperforms corrugated-laminated shale in terms of fracturing potential. As laminae increase, rock strength decreases, enhancing fracability, while thicker laminae hinder fracturing. The elastic modulus trend is clay minerals > calcite > quartz > pyrite, with Young's modulus negatively correlated with mineral deformation.*

Keywords: *uniaxial/triaxial test, nanoindentation, atomic force microscopy, fabric characteristics, mechanical properties.*

1. Introduction

As the world's second-largest energy consumer, China's dependence on foreign oil has long exceeded 70%, and the energy security situation is grim. According to estimates, China's geological resource potential of shale oil is 397.46×10^8 t, and the recoverable resource potential is 34.98×10^8 t, making shale oil and gas a key focus for future exploration and development [1–3]. Continental shale is characterized by wide distribution, relatively young geological age, simultaneous oil and gas generation, and great resource potential. It represents a favorable stratigraphic system for the stable storage and production of unconventional oil and gas [4].

---

* Corresponding author,

The Lianggaoshan Formation (Fm) shale in the Sichuan Basin has a wide distribution range, great resource potential, and high organic matter abundance. It is an ideal layer for shale oil and gas exploration and development. However, the heterogeneity of shale is strong and the mineral composition is complex, which shows strong mechanical anisotropy [5].

At present, the research and development of shale mechanical properties is progressing rapidly, and the technology is more advanced. In addition to the conventional uniaxial/triaxial macroscopic mechanical experiments, there are advanced microscopic nanoindentation experiments [6] and atomic force microscopy experiments [7]. Various experimental methods are used to explore the influencing factors of shale mechanical properties. Duan et al. [8] found that the heterogeneity of initial structural characteristics and the stress conditions of true triaxial loading jointly affect the crack propagation and failure mode of shale, the reduced stress ratio, and the fracture combination failure mode. The lamina is the basic unit of sedimentary bedding, and it is the smallest original sedimentary rock that can be distinguished by the naked eye on a macro scale. The mechanical response formed by different lamina characteristics varies [9]. Wei et al. [10] used scanning electron microscopy and other techniques to study shale bedding and fractures, and clarified the control mechanism of bedding development characteristics on the spatial distribution pattern of pores and fractures, as well as the influence of minerals on pores and fractures. Hua et al. [11] used a new layered division method based on XRF data to divide the laminated structure and mineral composition of the Qingshankou Formation shale in the Songliao Basin, indicating that the layered structure has an extremely important influence on reservoir quality. However, the microscopic fabric characteristics of layered shale are extremely complex. Xie et al. [12] found that the elastic modulus of pyrite particles is the highest, followed by quartz, feldspar, calcite, dolomite, clay minerals, and organic matter, by studying the mechanical properties of oriented shale from nanometer to micron scale.

Many scholars have studied the layered structure of shale, but the mechanical response and influencing factors of laminated shale in the Lianggaoshan Fm have not been clearly explored using both micro- and macro-mechanics experiments. Therefore, this study innovatively integrates a micro–macro multi-dimensional experimental system and systematically reveals the multi-scale mechanical response behavior of shale through nanoindentation, atomic force microscopy micromechanical testing, combined with uniaxial/triaxial compression and basic physical properties characterization. It focuses on the correlation between brittle mineral content and mechanical properties, the mechanical differences of various lamina morphological characteristics, the variation characteristics of shale mechanical properties under real formation confining pressure, the description of mineral fabric characteristics, and the influencing factors of the shale's micro-mechanical properties. This lays a theoretical foundation for the study of shale mechanical properties and their main controlling factors, and provides data support for shale oil mining and drilling fracturing technologies, providing new ideas for the exploitation of shale oil and gas.

2. Geological background

2.1. Geological environment

The Sichuan Basin is located in southwestern China, surrounded by the Longmen Mountains, Micangshan Mountains, Daba Mountains, etc., and contains both marine and continental two-phase strata. The Jurassic is the only key oil-bearing layer for exploration [13, 14]. The shale samples in this paper are taken from the Lianggaoshan Fm of the Aojiaying section, as shown in Figure 1a. The Lianggaoshan Fm shale is characterized by wide distribution, shallow burial depth, and abundant resources in the eastern Sichuan region [15]. Based on the detailed field outcrop measurements and considering the grain size and sedimentary structure of the rock, the Lianggaoshan Fm shale is divided into seven lithofacies: mudstone, shale, silty mudstone, argillaceous siltstone, siltstone, argillaceous fine sandstone, and fine sandstone, as shown in Figure 1b.

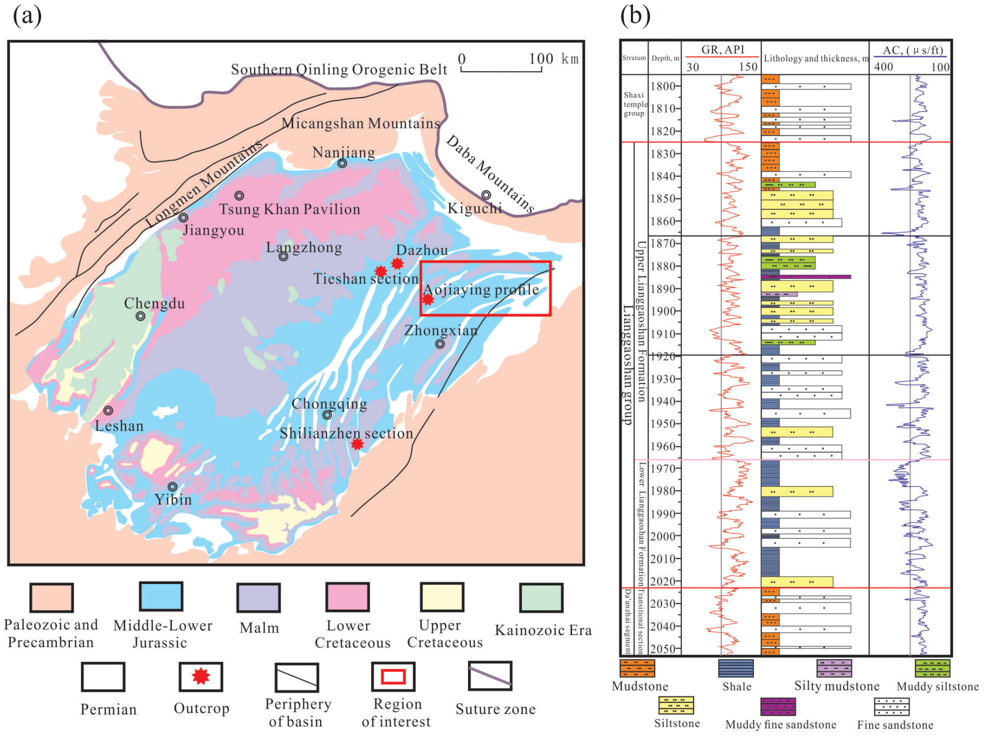

Fig. 1. Geological background of the study area (a) and stratigraphic histogram of the Lianggaoshan Formation (b).

Due to the complete delta–shore lake–shallow lake–semi-deep lake sedimentary cycle developed in the Lianggaoshan Fm, the properties of the parent rock have evolved from igneous rocks to metamorphic and sedimentary rocks. The source material is mainly from the Dabashan area and the southern Qinling Orogenic Belt [16]. Lamellar shale is widely developed, forming obvious mechanical anisotropy. The content of brittle minerals is high: quartz and feldspar constitute a brittle skeleton, and pyrite is concentrated in a strawberry-like form, which enhances local stress concentration and increases the likelihood of shear stress concentration [17, 18].

2.2. Sedimentary characteristics

The results of typical casting thin section identification show that the particle size of shale debris in the Lianggaoshan Fm ranges between 0.15–0.7 mm, mainly consisting of metamorphic rock. The fillings are argillaceous, calcite, siderite, and a small amount of pyrite, accompanied by a few intergranular dissolution pores and limited development of micro-fractures (Fig. 2a). The main reason is that, in the deep lake and semi-deep lake sedimentary system, the provenance is relatively far, the deposited shale is thick, and the organic matter content is high.

Because the samples in this paper are collected from field outcrops, the total organic carbon (TOC) content is determined to range between 0.97% and 1.03% due to the effects of weathering. However, there are also sedimentary facies with relatively close provenance, where shale thickness is reduced and sandy laminae are more developed [19]. As a result, muddy hydromica fills the intergranular spaces (Fig. 2b), showing a layered distribution; calcite cementation replaces clastic particles (Fig. 2c), and siderite agglomerates are present. The brittle mineral content in the shale is relatively high. The quartz content in samples Y1, Y2, and Y3 is 65%, 68%, and 72%, respectively.

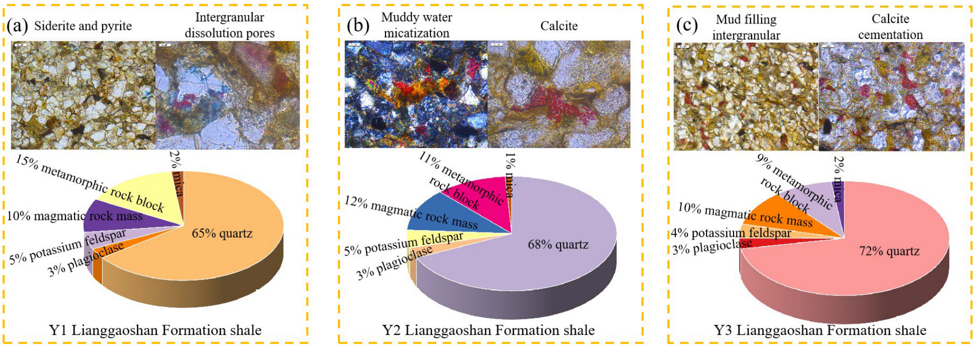

Fig. 2. Identification of Y1 (a), Y2 (b), and Y3 (c) casting thin sections of the Lianggaoshan Formation shale in eastern Sichuan.

2.3. Layer characteristics

According to the identification of thin sections in the study area, the shale is divided into two types of laminae: continuous laminae and discontinuous laminae [20]. The continuous laminae have good continuity and are mostly plate-like. The laminae are parallel, and the boundaries are clear. Bright and dark laminae appear alternately under single polarized light in the microscope. In the study area, the continuous laminae are characterized by straight, corrugated, and graded types.

The discontinuous laminae have poor continuity, with blurred and non-parallel interlamellar boundaries. Lenticular and irregular mineral assemblages can be observed under the polarizer. In the study area, the discontinuous laminae are characterized by lens-shaped, speckled, and weak types. A large number of micro-fissures are developed between the laminae, and star-shaped pyrite is distributed along the dark laminae.

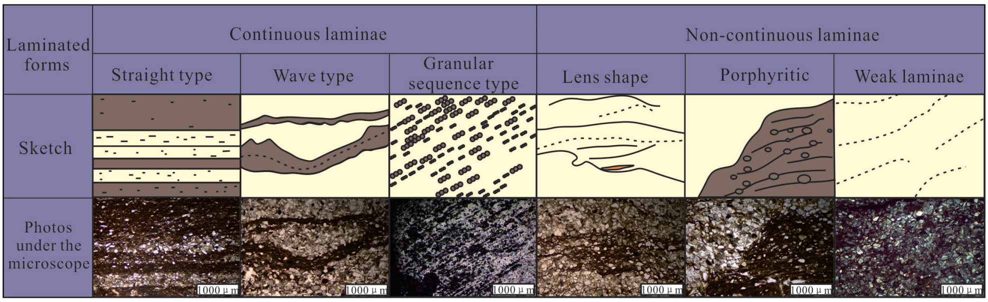

Fig. 3. Morphological sketch map of shale laminae and microscopic photos of the Lianggaoshan Formation in eastern Sichuan.

3. Experiments and methods

3.1. Uniaxial/triaxial rock mechanics

Flat-laminated and corrugated-laminated shale samples from the Lianggaoshan Fm were selected for uniaxial/triaxial experiments. The samples were core specimens with a diameter of 25 mm. The experimental instrument used was the GCTS-RTR1000 high-temperature and high-pressure triaxial rock mechanics test system. The experiment adopted the displacement control method, with a loading rate of 0.05 mm/min, and loading continued until the sample was destroyed.

Based on the geological characteristics of typical shale gas reservoirs buried at depths of 500–1500 m in China, and following the statistical law of ground stress gradient of 1.2–2.5 MPa/100 m, a confining pressure range of

5–15 MPa can effectively simulate the triaxial stress environment of an actual reservoir. The triaxial and uniaxial test equipment are the same. The confining pressure was set according to an arithmetic gradient of 5, 10, and 15 MPa. When the confining pressure reached the preset value, the axial loading rate was set to 0.03 mm/min until the sample was destroyed [21]. The experimental process is shown in Figure 4.

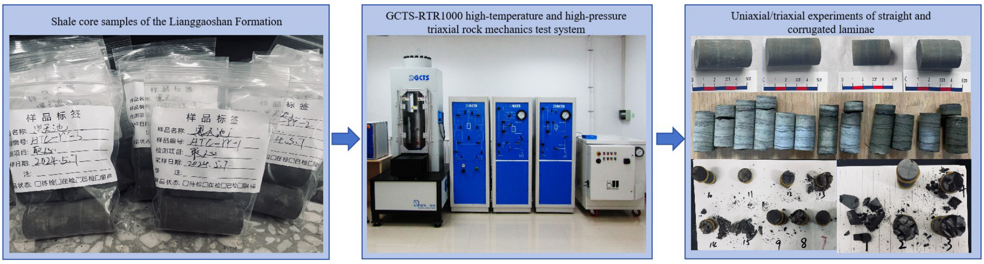

Fig. 4. Flow chart of uniaxial/triaxial experiments on Lianggaoshan Formation shale.

3.2. Nanoindentation experiment

The German Bruker TI 980 nanoindentation instrument was used, equipped with a triangular pyramid Brinell indenter with a curvature radius of 100 nm. Due to the high surface roughness of shale, the samples were cut, ground, and polished using argon ion. The polishing instrument was the Gatan argon ion polishing system Ilion II 697. Samples were cut into rectangular pieces of 10 × 10 × 3 mm, and a region with a radius of 1 mm was selected for polishing.

Within the polished circular area, dot positions were determined under the microscope. Based on the intensity and shape of the light reflected by the minerals, different mineral area arrays were selected for indentation. The experimental process is shown in Figure 5.

The experimental system used quasi-static indentation. The maximum load was 30 mN, with loading, holding, and unloading times of 10, 20, and 10 s, respectively. The longitudinal displacement noise background was less than 0.2 nm, and the thermal drift (at room temperature) was less than 0.05 nm/s. Using the classical Oliver–Pharr physical model, the elastic modulus (E) and hardness (H) of the sample were calculated, and the load–displacement curve was obtained [22].

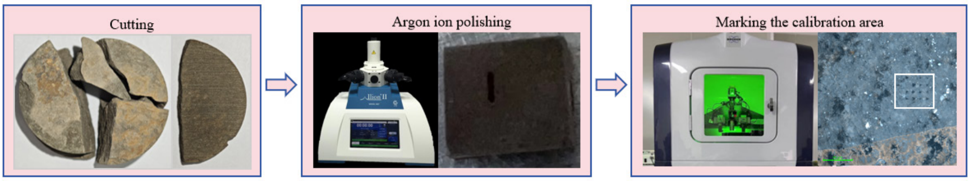

Fig. 5. Flow chart of the nanoindentation experiment on Lianggaoshan Formation shale.

3.3. Atomic force microscopy experiment

Based on the color, luster, and crystal form of minerals under the microscope, areas rich in pyrite, quartz, and clay minerals were selected for calibration, and the mechanical properties of different mineral components were studied using an atomic force microscope. Before the experiment, due to the high surface roughness requirements in atomic force microscopy experiment, the sample surface was cut, ground, and polished using argon ion [23]. The experimental process is shown in Figure 6.

The Bruker Dimension Icon AFM was used as the atomic force microscope. The test probe was RTESPA-525, with an elastic coefficient of 200 N/m and a tip radius of 8 nm. The scanning range of the atomic force microscope probe was 5 × 5 μm, with a scanning resolution of 256 × 256 points. The scanning speed was 0.5–1.0 Hz, and the modulus test range was 1–50 GPa.

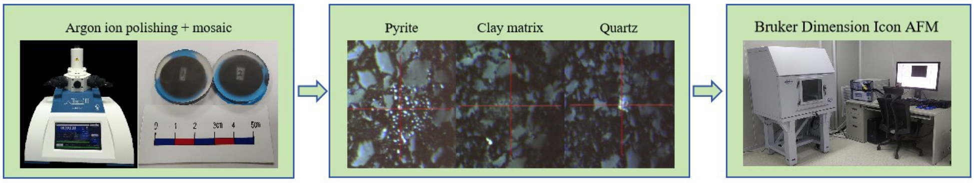

Fig. 6. Flow chart of the atomic force microscopy experiment on Lianggaoshan Formation shale.

4. Results and discussion

4.1. Effect of lamina characteristics on the mechanical properties of shale

There are differences in the density and morphology of shale laminae formed under different sedimentary environments [24]. The flat-stratified laminae are mainly formed by the semi-deep-sea subsidence, sedimentation of turbidity layers separated by the water column, and ocean sedimentation of eolian suspended matter [25]. The genesis of corrugated laminae is mainly due to resuspension. The overall mineral composition of this type of laminated shale is similar to that of flat laminae. The average content of quartz and feldspar is slightly higher than that of flat-laminated shale, while the content of pyrite and other minerals is relatively low [26].

The experimental results in this paper are shown in Figure 7. The elastic modulus of the flat-laminated shale in the uniaxial experiment ranges from 21.6 to 27.6 GPa. The elastic modulus of the corrugated-laminated shale in the uniaxial experiment ranges from 3.8 to 14.1 GPa, while in the triaxial experiment it ranges from 0.14 to 16.7 GPa.

The elastic modulus of the flat laminae under uniaxial conditions is generally higher than that of corrugated laminae and also higher than that of corrugated laminae under triaxial conditions. However, the elastic modulus of

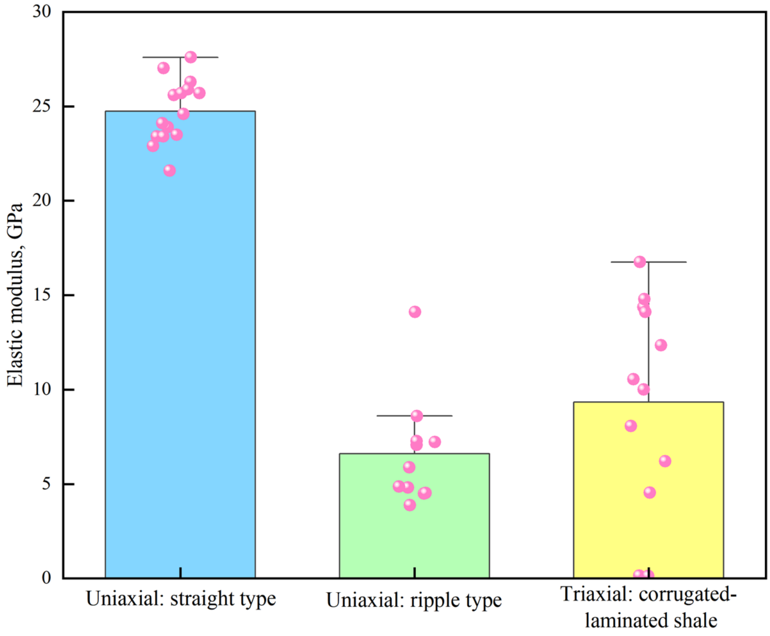

Fig. 7. Results of uniaxial/triaxial mechanical experiments on Lianggaoshan Formation shale.

corrugated-laminated shale under triaxial confining pressure is greater than that of corrugated-laminated shale under uniaxial conditions.

Figure 8 shows the stress–strain curves of straight and corrugated laminae before and after failure under nine sets of uniaxial and triaxial test conditions. Compared with Figure 8(a) (straight-layered shale), Figure 8(b) (corrugated-layered shale) demonstrates that the elastic modulus of straight laminated shale is larger, with the average elastic film content of 24.7 GPa, whereas that of corrugated-laminated shale is relatively small, with the average elastic film content of 6.6 GPa. The greater thickness of straight laminae increases the brittleness of the shale, and the mineral content of the laminae is also more brittle. It has more iron-bearing minerals, such as pyrite, and the laminae are fine, which is not conducive to the fracturing of the rock [27].

Based on the degree of lamina development observed in Figure 8(a), flat-laminated shale is further divided into three grades: I (1–3 laminae), II (3–6 laminae), and III (more than 6 laminae).

Comparing the elastic moduli of HY2, HY3, and HY12 from uniaxial experiments – 25.6, 23.9, and 22.9 GPa, respectively – the results show that the more developed the lamina, the lower the strength of the rock, and the better the fracturing. Xiong et al. [27] and other studies have shown that the number of laminae is generally inversely proportional to the compressive strength and elastic modulus of fine-grained sedimentary rocks, which confirms the experimental conclusions of this paper.

Table 1. Uniaxial/triaxial mechanical experimental data for Lianggaoshan Formation shale

Sample No.	Layer characteristics	Experiment	Elastic modulus	Poisson ratio
HY-1	Flat-stratified laminae	Uniaxial	27.03	0.25
HY-2	Flat-stratified laminae	Uniaxial	25.6	0.24
HY-3	Flat-stratified laminae	Uniaxial	23.9	0.21
HY-4	Flat-stratified laminae	Uniaxial	25.7	0.26
HY-5	Flat-stratified laminae	Uniaxial	23.4	0.21
HY-6	Flat-stratified laminae	Uniaxial	24.6	0.19
HY-7	Flat-stratified laminae	Uniaxial	23.5	0.21
HY-8	Flat-stratified laminae	Uniaxial	24.1	0.18
HY-9	Flat-stratified laminae	Uniaxial	25.7	0.19
HY-10	Flat-stratified laminae	Uniaxial	26.3	0.27
HY-11	Flat-stratified laminae	Uniaxial	23.4	0.25
HY-12	Flat-stratified laminae	Uniaxial	22.9	0.23
HY-13	Flat-stratified laminae	Uniaxial	25.9	0.29
HY-14	Flat-stratified laminae	Uniaxial	27.6	0.18
HY-15	Flat-stratified laminae	Uniaxial	21.6	0.26
Average			24.75	0.228
QY-2	Corrugated layer	Uniaxial	14.101	0.14
QY-11	Corrugated layer	Uniaxial	8.61	0.09
QY-13	Corrugated layer	Uniaxial	7.072	0.1
QY-18	Corrugated layer	Uniaxial	4.488	0.07
QY-20	Corrugated layer	Uniaxial	4.819	0.37
QY-21	Corrugated layer	Uniaxial	5.879	0
QY-22	Corrugated layer	Uniaxial	7.272	0.01
QY-24	Corrugated layer	Uniaxial	4.522	0
QY-25	Corrugated layer	Uniaxial	7.233	0.01
QY-26	Corrugated layer	Uniaxial	3.888	0.03
QY-27	Corrugated layer	Uniaxial	4.862	0.02
Average			6.61	0.076

Table 1. (continued)

Sample No.	Layer characteristics	Experiment	Elastic modulus	Poisson ratio
QY-1	Corrugated layer	Triaxial experiment	14.361	0.23
QY-3	Corrugated layer	Triaxial experiment	16.751	0.29
QY-5	Corrugated layer	Triaxial experiment	6.218	0.18
QY-6	Corrugated layer	Triaxial experiment	10.005	0.26
QY-7	Corrugated layer	Triaxial experiment	14.786	0.14
QY-8	Corrugated layer	Triaxial experiment	4.542	0.1
QY-9	Corrugated layer	Triaxial experiment	12.353	0.18
QY-12	Corrugated layer	Triaxial experiment	10.553	0.08
QY-4	Corrugated layer	Triaxial experiment	14.101	0.15
QY-14	Corrugated layer	Triaxial experiment	8.079	0.14
QY-10	Corrugated layer	Triaxial experiment	0.15	0.02
QY-23	Corrugated layer	Triaxial experiment	0.14	0.01
Average			9.34	0.15

Compared with Figure 8(b) and (c), the elastic modulus of shale increases with rising confining pressure. Specifically, the elastic moduli under confining pressures of 5, 10, and 15 MPa are 11.19, 12.35, and 14.02 GPa, respectively. Under the original uniaxial conditions, the average elastic modulus is 9.93 GPa. This indicates that under confining pressure, the gaps and microcracks between pores and mineral particles close, resulting in an increase in Young's modulus and a decrease in brittleness.

Rybacki et al. [28] and Zhang et al. [29] showed that when the confining pressure of shale is lower than 50 MPa, rising confining pressure leads to an increase in Young's modulus. This further confirms that the elastic modulus of corrugated-laminated shale under triaxial confining pressure is greater than under uniaxial conditions.

Xiaoqiong et al. [30] demonstrated that compared with straight-laminated shale, corrugated-laminated shale contains more naturally developed microcracks, exhibits lower compressive strength, and shows smaller fracture volume strain after failure. The main reason is that fractures in corrugated-

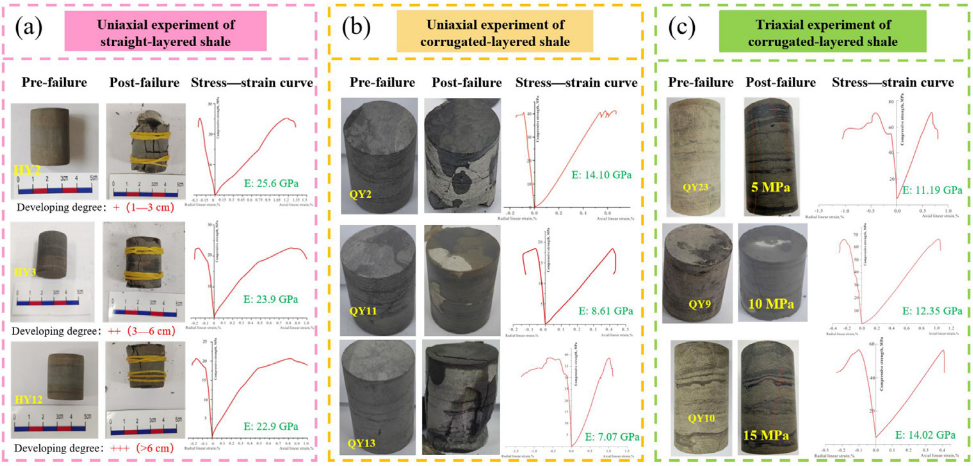

Fig. 8. Comparison of Lianggaoshan Formation shale before and after uniaxial/triaxial mechanical experiments.

laminated shale tend to have smaller apertures, which is consistent with the observed absence of an obvious fracture pressure drop on the field fracturing curve [31]. Therefore, increased confining pressure is not conducive to crack propagation and extension, and its compressive strength is stronger than that of corrugated-laminated shale. These results suggest that the application of confining pressure could be considered in the mining process technology.

4.2. Effect of mineral fabric on the mechanical properties of shale

The varying crystal structures of different mineral components lead to distinct mechanical responses. The load–displacement (P–h) curve obtained from the nanoindentation experiment captures the nonlinear mechanical response behavior between the indenter and the mineral during indentation [32]. In this paper, the locations of various minerals were determined under a microscope, and nanoindentation experiments were carried out accordingly. The experimental results are shown in Figure 9.

The elastic modulus distribution ranges for clay minerals, calcite, quartz, and pyrite were 9.66–25.74, 25.79–32.65, 32.61–47.78, and 41.56–64.08 GPa, respectively. The corresponding hardness distribution ranges were 0.063–0.99, 0.40–1.56, 0.61–2.75, and 1.24–7.94 GPa, respectively. The trend in average values was upward. The relationship between the elastic modulus and hardness of each mineral component was as follows: clay minerals > calcite > quartz > pyrite, which is consistent with previous research results [33]. The average elastic modulus values were 20.67 (clay minerals), 29.45 (calcite), 37.51 (quartz), and 52.43 GPa (pyrite), while the average hardness values were 0.53, 0.83, 1.35, and 3.65 GPa, respectively. At the same time, a small number of abnormal points were present, which may be attributed to the influence of pores, impurities, and defects that cause differences in mechanical properties.

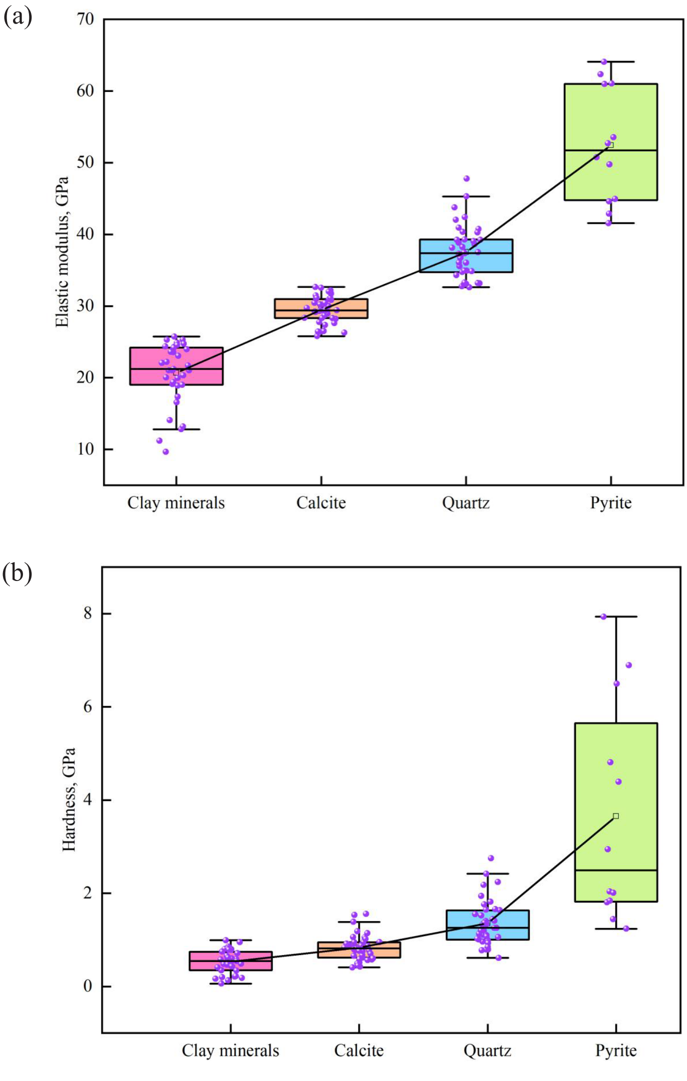

Fig. 9. Results of nanoindentation mechanical experiments on different mineral components of Lianggaoshan Formation shale: elastic modulus distribution (a) and hardness distribution (b).

Table 2. Statistical summary of nanoindentation mechanical experimental data for different mineral components in Lianggaoshan Formation shale

Test point	Mineral category	Elastic modulus, GPa	Hardness, GPa	Test point	Mineral category	Elastic modulus, GPa	Hardness, GPa
YY-1	Clay mineral	0.35	20.05	YY-63	Calcite	0.88	30.99
YY-2	Clay mineral	0.66	21.02	YY-64	Calcite	1.06	31.14
YY-3	Clay mineral	0.48	21.05	YY-65	Calcite	0.87	31.48
YY-4	Clay mineral	0.49	21.70	YY-66	Calcite	1.56	32.17
YY-5	Clay mineral	0.41	22.08	YY-67	Calcite	1.54	32.54
YY-6	Clay mineral	0.43	23.06	YY-68	Calcite	1.14	32.65
YY-7	Clay mineral	0.86	24.31	YY-69	Calcite	0.95	30.22
YY-8	Clay mineral	0.58	24.38	YY-70	Calcite	0.56	30.45
YY-9	Clay mineral	0.78	24.90	YY-71	Calcite	0.77	31.13
YY-10	Clay mineral	0.58	25.30	YY-72	Calcite	0.66	31.75
YY-11	Clay mineral	0.06	9.66	YY-73	Calcite	0.45	32.02
YY-12	Clay mineral	0.16	11.22	YY-74	Quartz	2.75	32.62
YY-13	Clay mineral	0.21	12.81	YY-75	Quartz	2.18	32.77
YY-14	Clay mineral	0.34	13.21	YY-76	Quartz	1.26	33.10
YY-15	Clay mineral	0.80	14.07	YY-77	Quartz	1.26	33.13
YY-16	Clay mineral	0.45	16.57	YY-78	Quartz	1.11	33.15
YY-17	Clay mineral	0.55	17.34	YY-79	Quartz	1.82	33.03
YY-18	Clay mineral	0.60	18.89	YY-80	Quartz	1.20	33.19
YY-19	Clay mineral	0.22	19.02	YY-81	Quartz	0.99	33.29
YY-20	Clay mineral	0.47	19.12	YY-82	Quartz	1.10	34.74
YY-21	Clay mineral	0.47	19.38	YY-83	Quartz	1.64	34.87
YY-22	Clay mineral	0.44	19.95	YY-84	Quartz	1.65	34.95
YY-23	Clay mineral	0.55	20.34	YY-85	Quartz	2.24	36.79
YY-24	Clay mineral	0.18	21.02	YY-86	Quartz	2.42	39.29
YY-25	Clay mineral	0.13	21.22	YY-87	Quartz	1.76	40.75
YY-26	Clay mineral	0.20	22.22	YY-88	Quartz	1.44	42.04
YY-27	Clay mineral	0.60	23.56	YY-89	Quartz	0.79	42.41
YY-28	Clay mineral	0.99	23.61	YY-90	Quartz	0.96	43.75
YY-29	Clay mineral	0.95	23.96	YY-91	Quartz	0.79	45.29
YY-30	Clay mineral	0.82	24.09	YY-92	Quartz	0.61	47.79

Table 2. (continued)

Test point	Mineral category	Elastic modulus, GPa	Hardness, GPa	Test point	Mineral category	Elastic modulus, GPa	Hardness, GPa
YY-31	Clay mineral	0.62	24.20	YY-93	Quartz	1.01	34.32
YY-32	Clay mineral	0.80	24.58	YY-94	Quartz	1.07	34.92
YY-33	Clay mineral	0.71	24.76	YY-95	Quartz	1.03	35.58
YY-34	Clay mineral	0.75	25.29	YY-96	Quartz	0.94	36.05
YY-35	Clay mineral	0.79	25.74	YY-97	Quartz	0.93	36.06
YY-36	Calcite	0.89	26.42	YY-98	Quartz	1.13	36.69
YY-37	Calcite	0.90	27.37	YY-99	Quartz	1.38	37.28
YY-38	Calcite	0.83	27.75	YY-100	Quartz	0.78	37.37
YY-39	Calcite	0.41	28.21	YY-101	Quartz	0.85	37.47
YY-40	Calcite	0.52	28.32	YY-102	Quartz	1.94	37.50
YY-41	Calcite	0.62	28.34	YY-103	Quartz	1.33	38.15
YY-42	Calcite	0.49	28.72	YY-104	Quartz	1.53	38.24
YY-43	Calcite	0.58	29.17	YY-105	Quartz	1.33	38.62
YY-44	Calcite	0.77	29.22	YY-106	Quartz	1.40	38.85
YY-45	Calcite	0.42	29.37	YY-107	Quartz	1.06	39.04
YY-46	Calcite	0.67	29.60	YY-108	Quartz	1.55	39.22
YY-47	Calcite	0.79	25.80	YY-109	Quartz	1.37	39.23
YY-48	Calcite	1.39	26.30	YY-110	Quartz	1.66	40.27
YY-49	Calcite	0.58	26.45	YY-111	Quartz	1.20	40.35
YY-50	Calcite	0.95	26.50	YY-112	Quartz	1.41	40.93
YY-51	Calcite	0.78	27.60	YY-113	Pyrite	6.90	50.74
YY-52	Calcite	0.95	28.36	YY-114	Pyrite	2.95	61.06
YY-53	Calcite	0.81	28.93	YY-115	Pyrite	1.24	52.72
YY-54	Calcite	0.89	29.31	YY-116	Pyrite	1.44	53.54
YY-55	Calcite	0.70	29.36	YY-117	Pyrite	2.04	60.96
YY-56	Calcite	0.84	29.43	YY-118	Pyrite	7.94	62.32
YY-57	Calcite	1.05	29.71	YY-119	Pyrite	6.50	64.09
YY-58	Calcite	1.18	30.02	YY-120	Pyrite	2.01	49.75
YY-59	Calcite	0.76	30.30	YY-121	Pyrite	4.39	41.56
YY-60	Calcite	0.60	30.46	YY-122	Pyrite	4.81	42.90
YY-61	Calcite	0.92	30.85	YY-123	Pyrite	1.81	44.60
YY-62	Calcite	1.02	30.97	YY-124	Pyrite	1.84	44.94

The load–displacement (P–h) curves of different minerals observed under the microscope show that, under the same load, pyrite exhibits the smallest displacement. During the unloading stage, pyrite recovers the greatest amount of elastic deformation, and its P–h curve dispersion is the smallest. The curves in both the loading and unloading stages are smooth, showing the stable mechanical properties of pyrite, and the corresponding mechanical parameter values are relatively high, as shown in Figure 10(d) and (e).

In comparison, quartz and calcite are more plastically deformed. As shown in Figure 10(a)–(e), their maximum displacements are significantly larger than those of pyrite. The "pop-in" phenomenon – caused by internal defects – leads to a sparse curve dispersion, and both the elastic modulus and hardness of these minerals are relatively lower [34]. Due to differences in lattice structures among mineral components, the spacing of load–displacement curves varies across

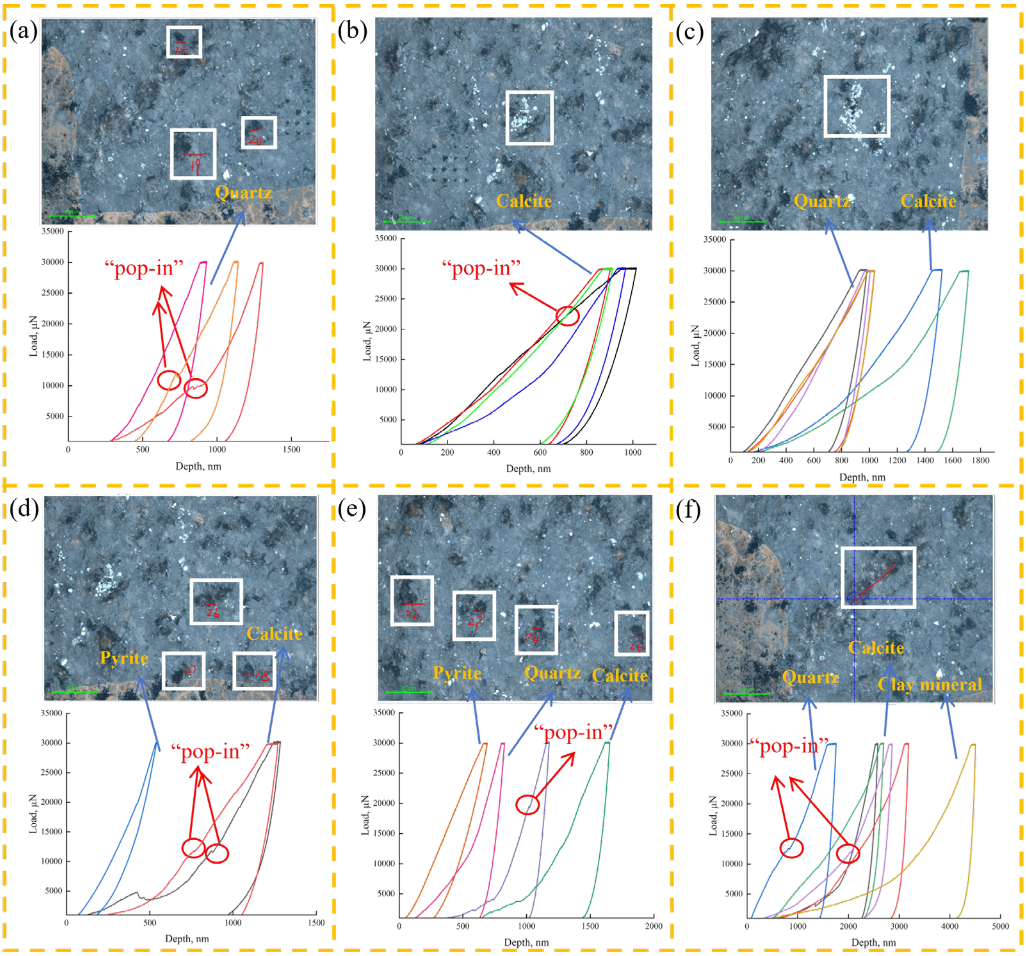

Fig. 10. Selected regions of different mineral components in Lianggaoshan Formation shale and the corresponding nanoindentation load–displacement curves.

minerals, and their surface pore–fracture characteristics differ accordingly. Even among the same mineral type, some variability in the load–displacement curves is observed, as shown in Figure 10(a) and (e). In Figure 10(f), the clay minerals exhibit the largest maximum displacement, as well as significant displacement during the holding load stage and residual stage, much greater than those of pyrite, quartz, and calcite.

Clay minerals exhibit strong plasticity. As they are mostly used as a filling material to fill the spaces between mineral particles, bending deformation of the force curve occurs during the plastic deformation stage, causing the end of the load–displacement curve to bend inward. The reason is that when the mineral particles are subjected to force, the force between the layer and the molecular structure changes the pore structure and shows strong heterogeneity [35]. Consequently, variations in mineral fabric characteristics [36], surrounding clay mineral content, uneven pore–fracture distribution, and surface roughness differences [37, 38] lead to variability in the micromechanical experimental results of the same mineral type.

Compared with quartz particles, calcite demonstrates poor thermal stability, and its yield platform appears earlier during the experiment. The mica-like layered structure shows a significant direction dependence during nanoindentation, which is closely related to the difference in the activation difficulty of the slip system. The load dispersion in clay mineral aggregates is significantly higher than that of quartz, which is consistent with the crystal strengthening mechanism [39]. Furthermore, under the influence of multi-scale co-evolutions, such as microcracks, the spacing of load–displacement curves varies across different minerals during micro/nanoindentation tests.

4.3. Atomic force mechanical response behavior of different minerals in oil shale

The mineral fabric characteristics control the mechanical response of minerals to atomic force, resulting in different atomic force mechanical parameters for different mineral components or even for varying morphological characteristics of the same mineral type [40]. As shown in Figure 11, the mechanical response curves of the same mineral are generally similar, with slight differences mainly caused by surface adhesion force. This adhesion force is affected by many factors such as surface energy, interfacial microstructure, and chemical composition. Additionally, the presence of surface pores increases the imbalance of force on the mineral surface – more pores correspond to higher adhesion force [41].

By comparing the force curves of pyrite (Fig. 11a), quartz (Fig. 11b), and clay minerals (Fig. 11c), it can be observed that the lowest point of the force curve for brittle minerals such as pyrite and quartz is relatively low, indicating high surface strength. In contrast, the force curve for clay minerals shows a higher minimum point, reflecting lower surface strength [42]. Due to the large surface color difference of clay mineral topography, high roughness, and

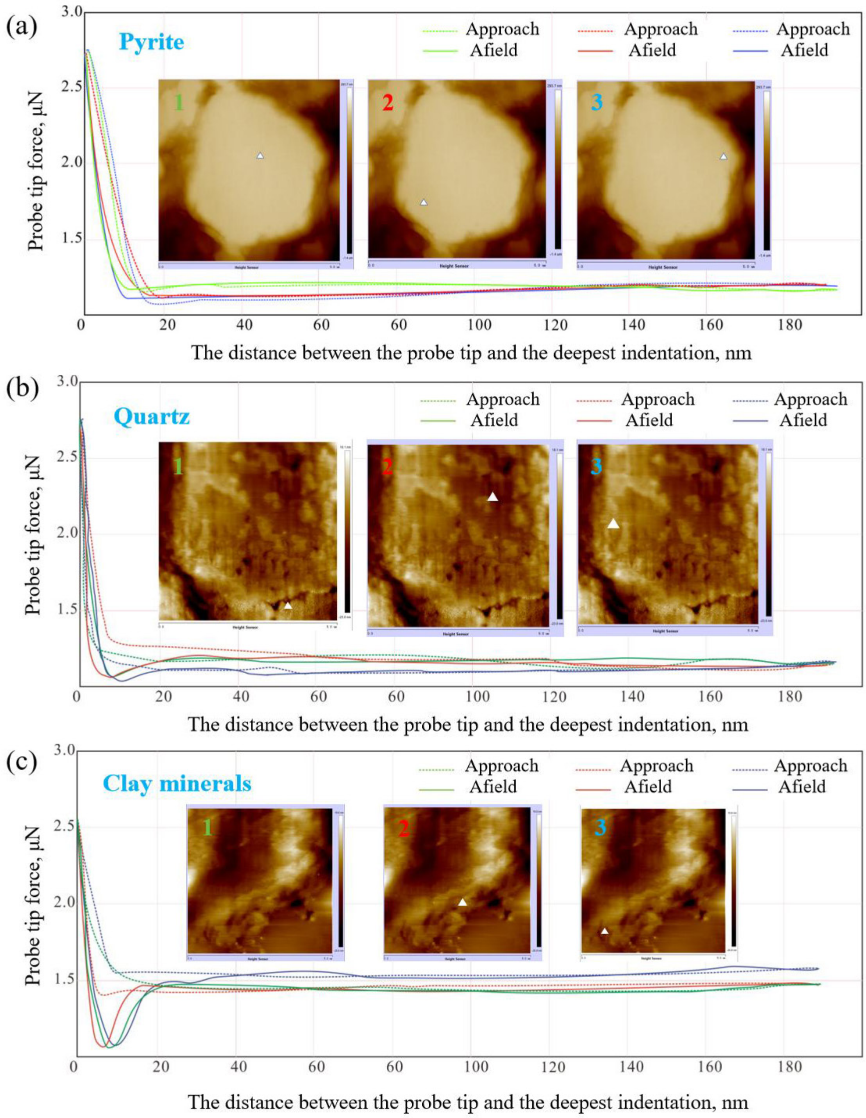

Fig. 11. Morphology (1, 2, 3) and atomic force curves of pyrite (a), quartz (b), and clay minerals (c) in Lianggaoshan Formation shale.

strong heterogeneity, the mechanical response curves display greater variation and reflect relatively weak surface mechanical properties [43].

According to Figure 12, the average Young's modulus values for pyrite, quartz, and clay minerals are 29.98, 19.89, and 4.44 GPa, respectively, indicating that pyrite and quartz possess relatively higher stiffness. The corresponding average deformations are 7.59 nm for pyrite, 13.18 nm for quartz, and 19.15

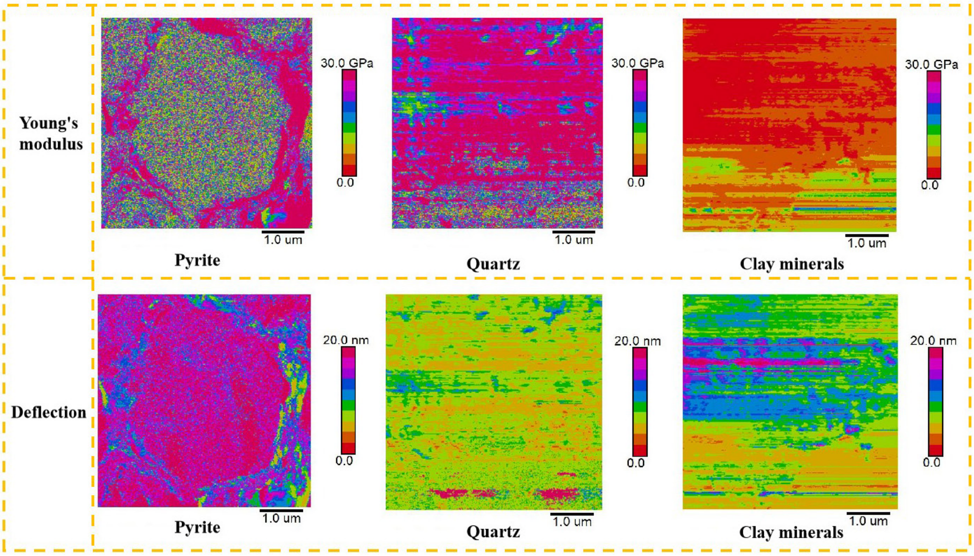

Fig. 12. Young’s modulus and deformation of pyrite, quartz, and clay minerals in Lianggaoshan Formation shale.

nm for clay minerals. Under the same applied pressure, pyrite and quartz exhibit lower deformation, while clay minerals show larger deformation. The content and type of minerals on the lamina surface influence shale fracture behavior under stress to a certain extent, providing data support for shale oil mining technologies. Yang et al. [44] found that the surface morphology and mineral distribution in shale seriously affect its failure modes: brittle minerals typically show serrated failure or point-like cracking, whereas plastic minerals mostly display the failure mode of debris accumulation on both sides.

Studies have shown that due to the small adhesion of minerals, probe deformation can be neglected, and the calculation results of Young’s modulus of minerals mainly depend on the extent of mineral deformation [45]. The maximum deformation of the sample comes from the elastic deformation and plastic deformation of the sample, and is related to hardness. When the deformation is plastic, the contact area and shape of the probe and the surface of the sample can be used to calculate the hardness value of the sample. In this paper, six groups of average values of deformation and six groups of average values of Young’s modulus are selected for fitting, corresponding to two sample surfaces, as shown in Figure 13. It is found that the Young’s modulus of different minerals in the two shale samples has a good correlation with the deformation. The Young’s modulus is negatively correlated with the deformation, and the fitting values are 0.67 and 0.99, respectively, which is consistent with previous studies and realizes the multi-directional application of each parameter [46].

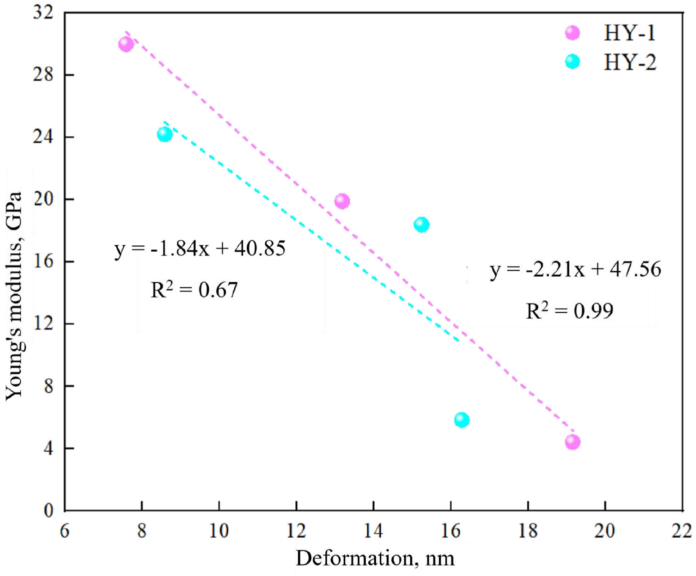

Fig. 13. Fitting diagram of Young's modulus and deformation for Lianggaoshan Formation shale.

5. Conclusion

In this paper, the mechanical properties and influencing factors of organic-rich oil shale in the Lianggaoshan Formation were studied through macroscopic and microscopic mechanical experiments. Based on the relationship between the proportion of brittle minerals, elastic modulus gradient, and lamina thickness affecting fracture propagation, a step-by-step injection scheme can be designed. In addition, a visual fracturing model can be developed during drilling, and different fracturing systems can be designed for varying mineral fabric characteristics. The following conclusions were obtained:

1. The organic-rich oil shale of the Lianggaoshan Formation in the study area contains a high proportion of brittle minerals. The laminae exhibit straight, corrugated, graded, lenticular, porphyritic, and weak forms. Numerous microcracks are developed between laminae, and star-shaped pyrite is distributed along the dark laminae. When the confining pressure is less than 50 MPa, the elastic modulus increases with rising confining pressure.
2. The mechanical properties of straight-laminated shale are higher than those of corrugated-laminated shale, and its fracturing ability is better.
3. Straight-laminated shale is divided into development grades I, II, and III. A greater number of laminae corresponds to lower rock strength and

improved fracturing potential. On the contrary, thicker laminae are less favorable for shale fracturing.

4. Nanoindentation experiments and mineral atomic force response analysis show that the relationship between the elastic modulus and hardness of different mineral components in Lianggaoshan Formation shale is as follows: clay minerals > calcite > quartz > pyrite. Young's modulus mainly depends on the extent of mineral deformation, and the two are negatively correlated.

Data availability statement

All data, models, and code generated or used during the study appear in the submitted article.

Acknowledgments

This study was supported by the study on fabric characteristics and multi-scale mechanical properties of shale oil reservoir (project No. HFKJ-CG-GJ-2024-05). The authors sincerely thank all reviewers for their critical and constructive comments. The publication costs of this paper were partially covered by the above fund project and partially by the Estonian Academy of Sciences.

References

1. Meng, Q. A., Lin, T. F., Zhang, J. Y., Liu, Z., Lu, J. C., Cheng, X. Y. In-situ accumulation process and reservoir characteristics of shale oil: a case study of Gulong shale oil in Songliao Basin. *Petroleum Geology and Oilfield Development in Daqing*, 2022, **41**(3), 24–37.
2. Guo, Q. L., Bai, X. F., He, W. J., Fan, L. Y., Wang, J., Jiang, W. Y. et al. Shale oil resource assessment methods, parameter standards and typical case studies. *China Petroleum Exploration*, 2022, **27**(5), 27–41.
3. Wang, Q. R., Tao, S. Z., Guan, P. Progress in research and exploration & development of shale oil in continental basins in China. *Natural Gas Geoscience*, 2020, **31**(3), 417–427. https://doi.org/10.11764/j.issn.1672-1926.2019.10.009
4. Fu, S. T., Jin, Z. J., Fu, J. H., Li, S. X., Yang, W. W. Transformation of understanding from tight oil to shale oil in the Member 7 of Yanchang Formation in Ordos Basin and its significance of exploration and development. *Acta Petrolei Sinica*, 2021, **42**(5), 561–569. http://dx.doi.org/10.7623/syxb202105001
5. Yan, B. H., Zhao, J. G., Xiao, Z. J., Zhong, Q. L., Ouyang, F., Wang, B. et al. Analysis of elastic properties and anisotropic rock physics modeling of Qianjiang

Formation shale. *Chinese Journal of Geophysics*, 2024, **67**(7), 2802–2819. https://doi.org/10.6038/cjg2022Q0724

6. Rahman, M. J., Lebedev, M., Mondol, N. H. Nanoscale mechanical properties of organic-rich Draupne caprock shale using nano-indentation method, offshore Norway. *International Journal of Greenhouse Gas Control*, 2024, **132**, 104073. https://doi.org/10.1016/j.ijggc.2024.104073
7. Zeng, Q., Wu, Y. K., Liu, Y. Q., Zhang, G. P. Determining the micro-fracture properties of Antrim gas shale by an improved micro-indentation method. *Journal of Natural Gas Science and Engineering*, 2019, **62**, 224–235. https://doi.org/10.1016/j.jngse.2018.12.013
8. Duan, Y. T., Zhu, C. C., Yang, B. C., Kong, R., Gu, L. J., Yu, L. Fracture propagation and failure mode characteristics of lamellar lacustrine shale under true triaxial compression conditions. *Environmental Earth Sciences*, 2024, **83**(3), 96. https://doi.org/10.1007/s12665-023-11390-4
9. Wu, S. T., Zhu, R. K., Luo, Z., Yang, Z., Jiang, X. H., Lin, M. J. et al. Laminar structure of typical continental shales and reservoir quality evaluation in central-western basins in China. *China Petroleum Exploration*, 2022, **27**(5), 62–72.
10. Wei, J. G., Li, J. T., Zhang, A, Shang, D. M., Zhou, X. F., Niu, Y. T. Influence of shale bedding on development of microscale pores and fractures. *Energy*, 2023, **282**, 128844. https://doi.org/10.1016/j.energy.2023.128844
11. Hua, G., Wu, S., Zhang, J., Liu, R., Guan, M., Cai, Y. et al. Laminar structure and reservoir quality of shales with high clay mineral content in the Qingshankou Formation, Songliao Basin. *Energies*, 2022, **15**(17), 6132. http://dx.doi.org/10.3390/en15176132
12. Xie, X. H., Deng, H. C., Hu, L. X., Li, Y., Mao, J. X., Liu, J. J. Assessing the effect of oriented structure characteristics of laminated shale on its mechanical behaviour with the aid of nano-indentation and FE-SEM techniques. *International Journal of Rock Mechanics and Mining Sciences*, 2024, **173**, 105625. https://doi.org/10.1016/j.ijrmms.2023.105625
13. Yang, X. J., Wang, M., Bai, X. F., Wang, X., Ying, Y. S., Li, T. Y. et al. Reservoir space characteristics and exploration of shale oil mobility of the Jurassic Lianggaoshan Formation shale in the northeastern Sichuan Basin. *Petroleum Science Bulletin*, 2024, **9**(2), 196–212.
14. He, W. Y., Bai, X. F., Meng, Q. A., Li, J. H., Zhang, D. Z., Wang, Y. Z. Accumulation geological characteristics and major discoveries of lacustrine shale oil in Sichuan Basin. *Acta Petrolei Sinica*, 2022, **43**(7), 885–898.
15. Zhang, J. X., Wang, Y. Z., Cheng, X. Q., Zhu, S. M, Zhu, Y. P. Geological characteristics of shale reservoirs and exploration potential of shale oil and gas in Jurassic Lianggaoshan Formation of northeastern Sichuan Basin. *Petroleum Geology and Development in Daqing*, 2025, **44**(2), 1–12.
16. Wang, D. J., Chen, C., Liu, Z. J., Yang, Z. J., Liu, M. M., Xie, J. T. Main controlling factors for oil and gas enrichment in Jurassic laminated shale in Fuxing area of Sichuan Basin. *Petroleum Geology & Experiment*, 2024, **46**(2), 319–332. http://dx.doi.org/10.11781/sysydz202402319

17. Zhao, Z. Y., Yan, C. L., Cheng, Y. F., Han, Z. Y., Xue, J. C. Study on the rock mechanical properties of Jurassic terrestrial reservoirs: a case study of the lower sub-section of the second section in Lianggaoshan Formation of the eastern Sichuan Basin. *Progress in Geophysics*, 2025, **40**(1), 266–275.
18. Wang, X., Wang, M., Zhao, C., Yang, X., Jia, Y., Wu, R. et al. Reservoir characteristics and controlling factors of the middle–high maturity multiple lithofacies reservoirs of the Lianggaoshan Formation shale strata in the northeastern Sichuan basin, China. *Marine and Petroleum Geology*, 2024, **161**, 106692. https://doi.org/10.1016/j.marpetgeo.2024.106692
19. Cheng, D. W., Zhang, Z. J., Hong, H. T., Zhang, S. M., Qin, C. Y., Yuan, X. J. et al. Sequence structure, sedimentary evolution and their controlling factors of the Jurassic Lianggaoshan Formation in the East Sichuan Basin, SW China. *Petroleum Exploration and Development*, 2023, **50**(2), 293–305. https://doi.org/10.1016/S1876-3804(23)60388-X
20. An, C., Liu, G. D., Sun, M. L., You, F. L., Wang, Z. X., Cao, Y. S. Development characteristics and classification of shale laminae in the Chang 7_3 sub-member of the Triassic Yanchang Formation in the Ordos Basin. *Petroleum Science Bulletin*, 2023, **8**(2), 125–140.
21. Huang, J. H., Li, X. L., Hu, G. Q., Zhang, W. Y., Zheng, L. G., Zhao, T., Jiang, C. X. Study on the Micro Macro Physical and Mechanical of Properties of Yangjialing Shale. *China Mine Engineering*, 2023, **52**(6), 6–11.
22. Wang, J. F., Yang, C., Liu, Y. K., Xiong, Y. Q. Review on the application of nanoindentation to study of shale mechanical property. *Oil & Gas Geology*, 2022, **43**(2), 477–488. https://doi.org/10.11743/ogg20220219
23. Wang, K. Y., Du, G. Study on the pore structure characteristics of shale by atomic force microscope and energy spectrum-scanning electron microscope. *Rock and Mineral Analysis*, 2020, **39**(6), 839–846. https://dx.doi.org/10.15898/j.cnki.11-2131/td.202004180053
24. Lazar, O. R., Bohacs, K. M., Macquaker, J. H. S., Schieber, J., Demko, T. M. Capturing key attributes of fine-grained sedimentary rocks in outcrops, cores, and thin sections: nomenclature and description guidelines. *Journal of Sedimentary Research*, 2015, **85**(3), 230–246. https://doi.org/10.2110/jsr.2015.11
25. O'Brien, N. R. Shale lamination and sedimentary processes. *Geological Society, London, Special Publications*, 1996, **116**, 23–36. https://doi.org/10.1144/GSL.SP.1996.116.01.04
26. Liu, Q., Yuan, X. J., Lin, S. H., Wang, L., Guo, H., Pan, S. Q. et al. The classification of lacustrine mudrock and research on its' depositional environment. *Acta Sedimentologica Sinica*, 2014, **32**(6), 1016–1025.
27. Xiong, Z. H., Cao, Y. C., Wang, G. M., Liang, C., Shi, X. M., Li, M. P. et al. Influence of laminar structure differences on the fracability of lacustrine fine-grained sedimentary rocks. *Acta Petrolei Sinica*, 2019, **40**(1), 74–85. https://doi.org/10.7623/syxb201901006
28. Rybacki, E., Reinicke, A., Meier, T., Makasi, M., Dresen, G. What controls the mechanical properties of shale rocks? – Part I: strength and Young's modulus.

Journal of Petroleum Science and Engineering, 2015, **135**, 702–722. https://doi.org/10.1016/j.petrol.2015.10.028

29. Zhang, Y. J., Chen, Z. P., Yu, C. Y., Dong, F., Qu, K. X., Shi, B. H. Geomechanical properties and influencing factors of organic-rich shale. *Mud Logging Engineering*, 2023, **34**(4), 104–111.
30. Xiaoqiong, W., Yi, Z., Youyu, W. et al. The influence of laminae on the mechanical properties of shale and its enlightenment to hydraulic fracturing. *Journal of China University of Petroleum (Natural Science Edition)*, 2025, **49**(1), 92–100.
31. Li, L., Huang, B., Huang, X., Wang, M., Li, X. Tensile and shear mechanical characteristics of Longmaxi shale laminae dependent on the mineral composition and morphology. *Energies*, 2020, **13**(11), 2977. https://doi.org/10.3390/en13112977
32. Ohmura, T., Wakeda, M. Pop-in phenomenon as a fundamental plasticity probed by nanoindentation technique. *Materials*, 2021, **14**(8), 1879. https://doi.org/10.3390/ma14081879
33. Xie, C. H., Deng, H. C., Hu, L. X., He, J. H., Li, R. X., Mao, J. X. et al. Investigation of the influence of shale bedding structure on its micro-macro mechanical behavior using nanoindentation and FE-SEM technology. *Geological Review*, 2024, **70**(S1), 319–322.
34. Timms, N. E., Healy, D., Reyes-Montes, J. M., Collins, D. S., Prior, D. J., Young, R. P. Effects of crystallographic anisotropy on fracture development and acoustic emission in quartz. *Journal of Geophysical Research: Solid Earth*, 2010, **115**(B7). http://dx.doi.org/10.1029/2009JB006765
35. Cao, F., He, J. H., Cao, H. X., Deng, H. C., Jiang, R., Wang, W. et al. Multi-scale rock mechanical parameters and quantitative assessment of brittleness in alkaline lacustrine shale reservoirs. *Journal of Chengdu University of Technology (Natural Science Edition)*, 2025, 1–18. https://dx.doi.org/10.12474/cdlgzrkx.2024080301
36. Zhao, Y. L., Luo, M. Y., Liu, L. F., Wu, J. F., Chen, M., Zhang, L. H. Molecular dynamics simulations of shale gas transport in rough nanopores. *Journal of Petroleum Science and Engineering*, 2022, **217**, 110884. https://doi.org/10.1016/j.petrol.2022.110884
37. Huang, B. X., Li, L. H., Tan, Y. F., Hu, R. L., Li, X. Investigating the meso-mechanical anisotropy and fracture surface roughness of continental shale. *Journal of Geophysical Research: Solid Earth*, 2020, **125**(8), e2019JB017828. https://doi.org/10.1029/2019JB017828
38. Yu, H., Shen, R., Guo, H. K., Wang, G., Shao, G., Shang, Z. Characterization of pore structure of shale by atomic force microscopy. *Science and Technology and Engineering*, 2022, **22**(36), 16016–16023.
39. Rashid, F., Singh, D. N. Discussion on the paper "Thermal effects promotes non-Darcian flow in heated rock fractures" by Jie Tan, Guan Rong, Changdog Li, Jia-Qing Zhou, and Huiming Tang 2023. *Rock Mechanics and Rock Engineering*, 2024, **57**, 2289–2291. https://doi.org/10.1007/s00603-023-03641-4
40. Zhang, M. Z., Xu, J. J., Jiang, Q., Tang, H. X., Wang, Z. Z., Zhang, Y. H. et al. Cross-scale characterization of the Young's modulus of slate using atomic force microscopy. *Rock and Soil Mechanics*, 2022, **43**(S1), 245–257.

41. Tang, X. Study on nano-micro mechanical properties of coal rock: taking Pocahontas coal rock as an example. *Coal Science and Technology*, 2020, **48**(2), 220–229.
42. Xu, J. J., Tang, X. H., Wang, Z. Z., Feng, Y. F., Bian, K. Investigating the softening of weak interlayers during landslides using nanoindentation experiments and simulations. *Engineering Geology*, 2020, **277**, 105801. https://doi.org/10.1016/j.enggeo.2020.105801
43. Cai, X., Xia, W., Liu, H. R., Liu, L., Lu, C. X., Liu, Y. X. Discussion on the innovative application of atomic force microscope in the microscopic characterization of shale. *China Plant Engineering*, 2021, **43**(S1), 229–232.
44. Yang, L., Yang, D., He, M. C. Quantitative study on distribution range of interface transition zone in continental shale beddings based on nano scratch. *Rock and Soil Mechanics*, 2025, **46**(2), 353–367.
45. Moro, D., Ulian, G., Valdrè, G. Nanoscale cross-correlated AFM, Kelvin probe, elastic modulus and quantum mechanics investigation of clay mineral surfaces: the case of chlorite. *Applied Clay Science*, 2016, **131**, 175–181. https://doi.org/10.1016/j.clay.2015.11.023
46. Iferobia, C. C., Ahmad, M. Nanoindentation application in geomechanics analysis of shale under high-temperature treatment/thermal fracturing conditions. *Bulletin of Engineering Geology and the Environment*, 2023, **82**(12), 453. https://doi.org/10.1007/s10064-023-03460-5